The Astrophysical Journal, 614:301–308, 2004 October 10

A DECREASING COLUMN DENSITY DURING THE PROMPT EMISSION FROM GRB 000528 OBSERVED WITH *BeppoSAX*

F. Frontera,[1,2] L. Amati,[2] D. Lazzati,[3] E. Montanari,[1,4] M. Orlandini,[2] R. Perna,[5] E. Costa,[6] M. Feroci,[6] C. Guidorzi,[1] E. Kuulkers,[7] N. Masetti,[2] L. Nicastro,[8] E. Palazzi,[2] E. Pian,[9] and L. Piro[5]

Received 2004 June 1; accepted 2004 June 15

ABSTRACT

We report observation results of the prompt X- and gamma-ray emission from GRB 000528. This event was detected with the Gamma-Ray Burst Monitor and one of the two Wide Field Cameras aboard the *BeppoSAX* satellite. The gamma-ray burst (GRB) was promptly followed on with the *BeppoSAX* narrow field instruments and with ground optical and radio telescopes. The X-ray afterglow source was identified, but no optical or radio counterpart found. We report here results from the prompt and afterglow emission analysis. The main feature derived from spectral evolution of the prompt emission is a high hydrogen equivalent column density with evidence of its decrease with time. We model this behavior in terms of a time-dependent photoionization of the local circumburst medium, finding that a compact and dense environment is required by the data. We also find a fading of the late part of the 2–10 keV prompt emission, which is consistent with afterglow emission. We discuss this result in the light of the external shock model scenario.

Subject headings: gamma rays: bursts — gamma rays: observations — X-rays: bursts

1. INTRODUCTION

The prompt emission of long duration (>2 s) gamma-ray bursts (GRBs) in the broad 2–700 keV energy band, which was accessible to the *BeppoSAX* wide field instruments (Wide-Field Cameras, Jager et al. 1997; Gamma-Ray Burst Monitor, Frontera et al. 1997), has been demonstrated to provide information not only on the X-ray emission mechanisms of GRBs but also on their environments (e.g., Frontera et al. 2000, Frontera 2004). The properties of these environments are of key importance to unveil the nature of the GRB progenitors, which is a still open issue. Many observational results point to the collapses of massive stars, in particular to the explosions of Type Ic supernovae, as the most likely progenitors of long GRBs. However, the question of whether the GRB event and supernova explosion are simultaneous for all GRBs (hypernova model, e.g., Paczynski 1998), in spite of the convincing results obtained from GRB 030329 (Stanek et al. 2003; Hijorth et al. 2003), is still open. A two-step process, in which the massive star first gives rise to a supernova explosion with the formation of a neutron star and then, after some time, to a GRB from the delayed collapse of the neutron star to a black hole (supranova model, Vietri & Stella 1998) or from a phase transition to quark matter (Berezhiani et al. 2003) cannot be robustly excluded. At least in some cases (e.g., GRB 990705, Amati et al. 2000; GRB 011211, Frontera et al. 2004; GRB 991216, Piro et al. 2000), those in which X-ray transient absorption features or emission lines have been observed and found to be consistent with an iron-enriched environment typical of a previous supernova explosion, the two-step process is favored (Lazzati et al. 2001a, 2001b, 2002).

The properties of the GRB environment can also be derived from the study of the continuum spectrum of the prompt X-ray emission, which is expected to show a low-energy cutoff in the case of a high column density along the line of sight. If the absorbing material is located between a fraction of a parsec and several parsecs from the GRB site, the cutoff is expected to fade as the GRB evolves, as a result of the progressive photoionization of the gas by the GRB photons (e.g., Böttcher et al. 1999; Lazzati & Perna 2002). This is an effect analogous to the one originally proposed by Perna & Loeb (1998) in the optical domain with resonant lines. In fact, such cutoffs, in addition to evidence of their decreasing behavior with time from the GRB onset, have already been detected (GRB 980506, Connors & Hueter 1998; GRB 980329, Frontera et al. 2000). Lazzati & Perna (2002) interpreted them as evidence for the presence of overdense regions in molecular clouds with properties similar to those of star formation globules.

Now we report the discovery of another case of absorption. It has been found in the X-ray spectrum of the prompt emission of GRB 000528, in the context of a systematic investigation (F. Frontera et al. 2004, in preparation) performed to study the spectral evolution of all GRBs jointly detected with the *BeppoSAX* WFCs and the GRBM. GRB 000528, detected with the GRBM (Guidorzi et al. 2000) and localized with one of the two WFCs (Gandolfi 2000), was promptly followed up with the *BeppoSAX* Narrow Field Instruments (NFI), with the discovery in the WFC error box of a likely X-ray afterglow candidate of the burst (Kuulkers et al. 2000). However, neither an optical nor radio counterpart was found (lowest upper limit to the R magnitude of 23.3, Palazzi et al. 2000; 3.5 σ upper limit of 0.14 mJy at 8.46 GHz, Berger & Frail 2000).

[1] Physics Department, University of Ferrara, Via Paradiso 12, 44100 Ferrara, Italy; frontera@fe.infn.it.
[2] Istituto Astrofisica Spaziale e Fisica Cosmica, Section of Bologna, CNR, Via Gobetti 101, 40129 Bologna, Italy.
[3] Institute of Astronomy, University of Cambridge, Madingley Road, Cambridge CB3 0HA, UK.
[4] Also at: ISA "Virgili," Moderno, Italy.
[5] Department of Astrophysics, University of Princeton University, Peyton Hall, Ivy Lane, Princeton, NJ 08544-0001.
[6] Istituto Astrofisica Spaziale e Fisica Cosmica, CNR, Via Fosso del Cavaliere, 00133 Roma, Italy.
[7] European Space Research and Technology Center, ESA, Keplerlaan 1, NL-2200 AG Noordwijk, Netherlands.
[8] Istituto Astrofisica Spaziale e Fisica Cosmica, Section of Palermo, CNR, Via U. La Malfa 153, 90146 Palermo, Italy.
[9] Osservatorio Astronomico di Trieste, INAF, Trieste, Italy.

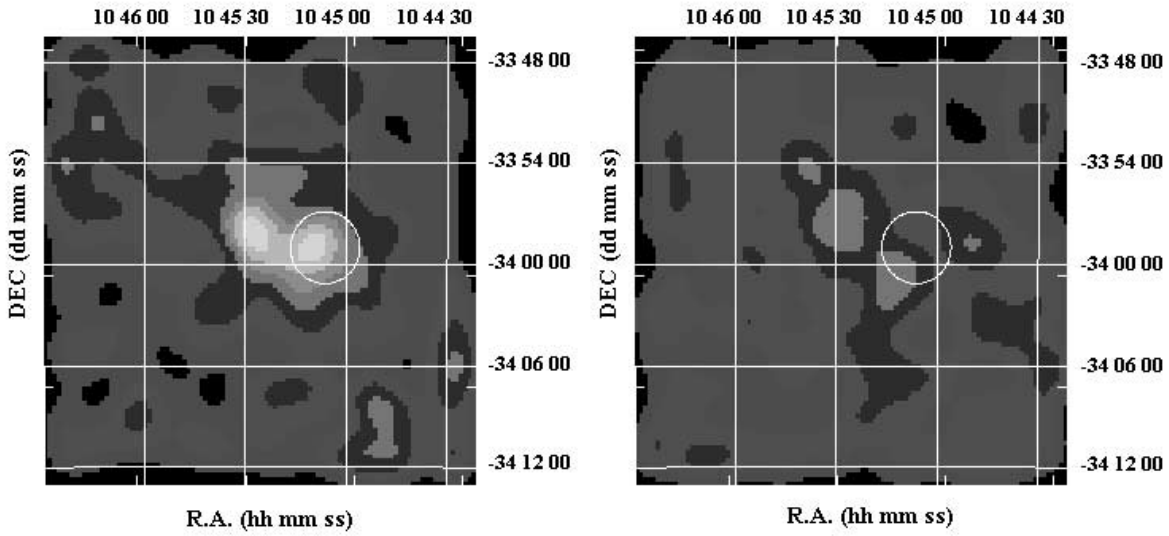

FIG. 1.—The 2–10 keV images of the sky field obtained with MECS in the two *BeppoSAX* follow–up observations of GRB 000528. The first ToO started 8.25 hr after the burst, the second 3.284 days later. The error box obtained with the WFC 2 is also shown.

In this paper we report our findings and their interpretation. We also discuss the follow-up X-ray observations performed with the *BeppoSAX* NFIs and their implications.

2. *BeppoSAX* OBSERVATIONS

GRB 000528 was detected with the *BeppoSAX* WFC 2 and the GRBM (Gandolfi 2000) on 2000 May 28 at 08:46:21 UT. The GRB position was determined with an error radius of 2′ (99% confidence level) and was centered at $\alpha_{2000} = 10^{\rm h}45^{\rm m}06\overset{\rm s}{.}3$, $\delta_{2000} = -33^\circ58'59''$ (in 't Zand et al. 2000). The burst was then followed up with the NFIs two times, the first time (ToO1) from May 28.71 UT to May 29.57 UT (from 8.25 to 28.90 hr after the main event) and the second time (ToO2) from May 31.65 UT to June 1.49 UT (from 3.284 to 4.124 days from the main event). Two previously unknown sources, the first (S1) designated 1SAX J1045.5−3358, with coordinates $\alpha_{2000} = 10^{\rm h}45^{\rm m}28^{\rm s}$, $\delta_{2000} = -33^\circ58'14''$, and the second (S2) designated 1SAX J1045.1−3358, with coordinates $\alpha_{2000} = 10^{\rm h}45^{\rm m}08^{\rm s}$, $\delta_{2000} = -33^\circ59'26''$, were detected with MECS and both were found to have disappeared in ToO2 (Kuulkers et al. 2000). However, only the S2 position (uncertainty radius of 1.5′) was found to be consistent with the WFC error box (see also Hurley et al. 2000).

We have reanalyzed the MECS and LECS data. The exposure times of the two instruments to the GRB direction are 8084 s (LECS) and 26,589 s (MECS) in ToO1 and 6905 s (LECS) and 31,210 s (MECS) in ToO2. The images of the sky field derived with MECS 2+3 during the two ToOs are shown in Figure 1, with the WFC error box superposed. The two sources reported by Kuulkers et al. (2000) are clearly visible in the left image. The probability that the excesses found are due to background fluctuations is $\sim 7 \times 10^{-7}$. The source S1, which is out of the WFC error box, is coincident with a radio source that was already present in the NRAO VLA Sky Survey at the time of the GRB occurrence. It was again detected by Berger & Frail (2000) during the search for the radio counterpart of GRB 000528. This source is also detected in the second *BeppoSAX* NFI observation (chance probability of $\sim 5 \times 10^{-4}$) with a flux variation of a factor of 1.7 from the first to the second ToO. However, the source S2 is detected only during the first ToO, it is consistent with the WFC position, and it undergoes a flux decrease larger than a factor of 3 from the first to the second ToO (see § 3.2). As already concluded by Kuulkers et al. (2000), we assume this object to be the likely afterglow source of GRB 000528.

3. DATA ANALYSIS AND RESULTS

The spectral analysis of both the prompt and afterglow emission was performed with the XSPEC software package (Arnaud 1996), version 11.2. All the reported parameter uncertainties are given at 90% confidence level.

3.1. *Prompt Emission*

Data available from the GRBM include 1 s ratemeters in the two energy channels (40–700 keV and >100 keV), 128 s count spectra (40–700 keV, 225 channels), and high time resolution data (up to 0.5 ms) in the 40–700 keV energy band. WFCs were operated in normal mode with 31 energy channels in 2–28 keV and 0.5 ms time resolution. The burst direction was offset by $8\overset{\circ}{.}0$ with respect to the WFC axis. With this offset, the effective area exposed to the GRB was $\sim$340 cm^2 in the 40–700 keV band and 70 cm^2 in the 2–28 keV energy band. The background in the GRBM energy band was estimated by linear interpolation using the 250 s count rate data before and after the burst. The WFC spectra were extracted through the Iterative Removal of Sources procedure (IROS,[10] e.g., Jager et al. 1997), which implicitly subtracts the contribution of the background and of other point sources in the field of view.

Figure 2 shows the light curve of GRB 000528 in two energy bands. In X-rays (Fig. 2, *top panel*) it shows a seemingly long rise superposed with various small pulses until it achieves the highest peak at a level of 300 counts s^{-1} after $\sim$70 s from the onset. Then the X-ray flux starts to smoothly decay and ends after $\sim$120 s from the flux peak. In gamma rays the light curve (*bottom panel*) is totally different. Corresponding to the first of the secondary pulses of the X-ray light curve we find the most prominent gamma-ray pulse, where the GRB achieves the maximum count rate of 1700 counts s^{-1} in the 40–700 keV band. Instead, corresponding to the

[10] WFC software version 105.108.

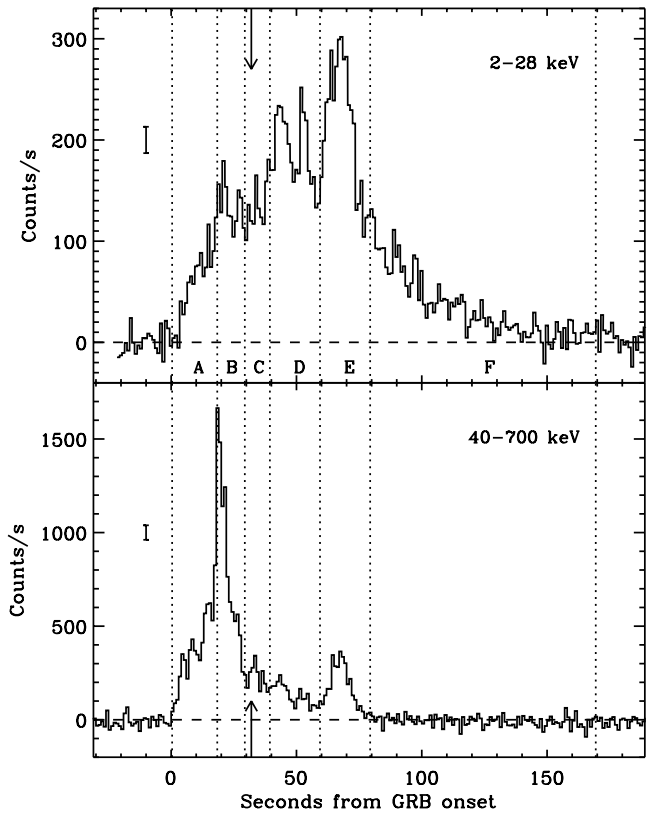

FIG. 2.—Light curve of GRB 000528 in two energy bands, 2–28 keV (WFC) and 40–700 keV (GRBM), after background subtraction. The zero abscissa corresponds to 2000 May 28, 08:46:21 UT. The time slices over which the 2–700 keV spectral analysis was performed using the 1 s GRBM counters are indicated by vertical dashed lines. The two time slices (named 1 and 2 in the text) for which the 225 channel GRBM spectra were also available are separated by a vertical arrow.

peak flux in X-rays we only find a secondary pulse of the gamma-ray light curve. Smaller and shorter duration pulses are also visible in the gamma-ray light curve. However, the smooth decay of the X-ray light curve is not observed in gamma rays, and the entire duration of the 40–700 keV burst is only ~80 s versus the ~160 s duration in X-rays.

For the study of the GRB spectral shape and its evolution with time, we extracted the WFC and GRBM data in the same time intervals, and we simultaneously fitted the WFC and GRBM data. For the GRBM we used both types of data available, the 1 s counters and the 128 s spectra. Using the counters it was possible to subdivide the GRB light curve in six adjacent time intervals A, B, C, D, E, and F of 18, 11, 10, 20, 20, and 90 s durations, respectively (see Fig. 2), and to derive 2–700 keV count spectrum for each of these intervals. The obtained GRB count spectra are shown in Figure 3. Given that the first three spectra (A, B, and C) have a low statistical quality in the 2–28 keV band, for the fitting analysis they were summed together (interval ABC). Using 128 s GRBM transmitted spectra, we obtained two 2–700 keV spectra in the two time intervals 1 and 2, whose boundary time is marked in Figure 2. The interval 1 covers most of the ABC interval above, while the interval 2 covers the intervals D, E, and F.

Each of the four spectra (ABC, D, E, and F) was fit with various continuum models: a power law (PL), a power law with an exponential cutoff (CPL), a broken power law (BKNPL), and a smoothly broken power law (or Band law, BL; Band et al. 1993). All these models were assumed to be photoelectrically absorbed by an equivalent hydrogen column density $N_{\rm H}$ to be determined (the WABS model in XSPEC). In the fits, the normalization factor of the GRBM data with respect to the WFC was left free to vary, checking that its best-fit value was in the range (0.8–1.3) in which this parameter was found in the flight calibrations with either celestial sources (e.g., Crab Nebula) or GRBs observed with both the WFC-GRBM and the BATSE experiment aboard the *Compton Gamma Ray Observatory* (e.g., Fishman et al. 1994). The power-law model gave a completely unacceptable fit of all count spectra either assuming the Galactic column density along the GRB line of sight ($N_{\rm H}^G = 6.1 \times 10^{20}$ cm^{-2}) or leaving $N_{\rm H}$ free to vary in the fit. The fit with the Band law gave, in general, unconstrained parameters. The other two models, CPL and BKNPL, turned out to be the most suitable to describe the data. The fit results with these models are reported in Table 1, along with the χ^2/dof value either in the case that $N_{\rm H}$ is frozen to the Galactic value ($N_{\rm H}^G$) or in the case that it is left free to vary in the fit.

Apart from the typical hard-to-soft evolution of the spectrum with time, the most remarkable feature found is the value of the column density $N_{\rm H}$, which turns out to be higher than the Galactic value in the first three time intervals ABC, D, and E (see chance probabilities obtained with *F*-test in Table 1) and is consistent with 0, and thus with $N_{\rm H}^G$, in the interval F (2 σ upper limit reported in Table 1). As can be seen from the *F*-test values, these results are independent of the spectral model chosen (BKNPL or CPL). We notice that, although with lower significance, these results are confirmed with fits using WFC data only. In addition, the analysis of the two GRBM 128 s spectra are consistent with these results. Both spectra were well fitted with either a BKNPL or CPL. In both cases a column density $N_{\rm H} = N_{\rm H}^G$ does not give the best description of the data (see Table 1); a best fit is obtained with $N_{\rm H}$ values significantly higher than the Galactic column density.

Even if we cannot completely exclude a constantly high $N_{\rm H}$, the data are in favor of a decreasing column density. Indeed, summing together the data in the intervals ABC and D, we estimate an $N_{\rm H} = \left(1.0^{+0.4}_{-0.3}\right) \times 10^{23}$ cm^{-2}, which is not consistent with the highest 2 σ upper limit of $N_{\rm H}$ in interval F (4.4×10^{22} cm^{-2}) and is only marginally consistent with its 3 σ upper limit. In addition, we find that the $N_{\rm H}$ centroid is continuously decreasing with time (see Fig. 4), and the fit of the $N_{\rm H}$ values with a constant [weighted mean value $(5.8 \pm 1.1) \times 10^{23}$ cm^{-2}] gives a χ^2/dof value of 7.8/3, versus a value of 0.65/2 in the case of an exponential law [$N_{\rm H}(t) = N_0 \exp(-t/t_0)$]. Using the *F*-test (Bevington 1969), the probability that a constant $N_{\rm H}$ value is the real parent distribution is 6%. Finally the comparison of the light curves in the 2–10 keV and 10–28 keV energy bands (Fig. 4) is also suggestive of a variable $N_{\rm H}$. Assuming the above exponential law, the best-fit parameters of the exponential law are $N_0 = (2.4 \pm 1.2) \times 10^{23}$ cm^{-2} and $t_0 = 51 \pm 23$ s.

No evidence of an absorption edge associated with the variable $N_{\rm H}$ is found in the spectra. The upper limit to the edge optical depth τ depends on the energy assumed and on the time interval considered. With the continuum parameters fixed to their best-fit values obtained with the CPL, the 2 σ τ upper limit achieves the lowest value (0.2) at 5 keV in interval D and the highest value (1.8) at 2 keV in the interval ABC. The other upper limits are in between.

On the basis of the best-fit results, peak fluxes and fluences associated with the event were derived. The 2–10 keV and

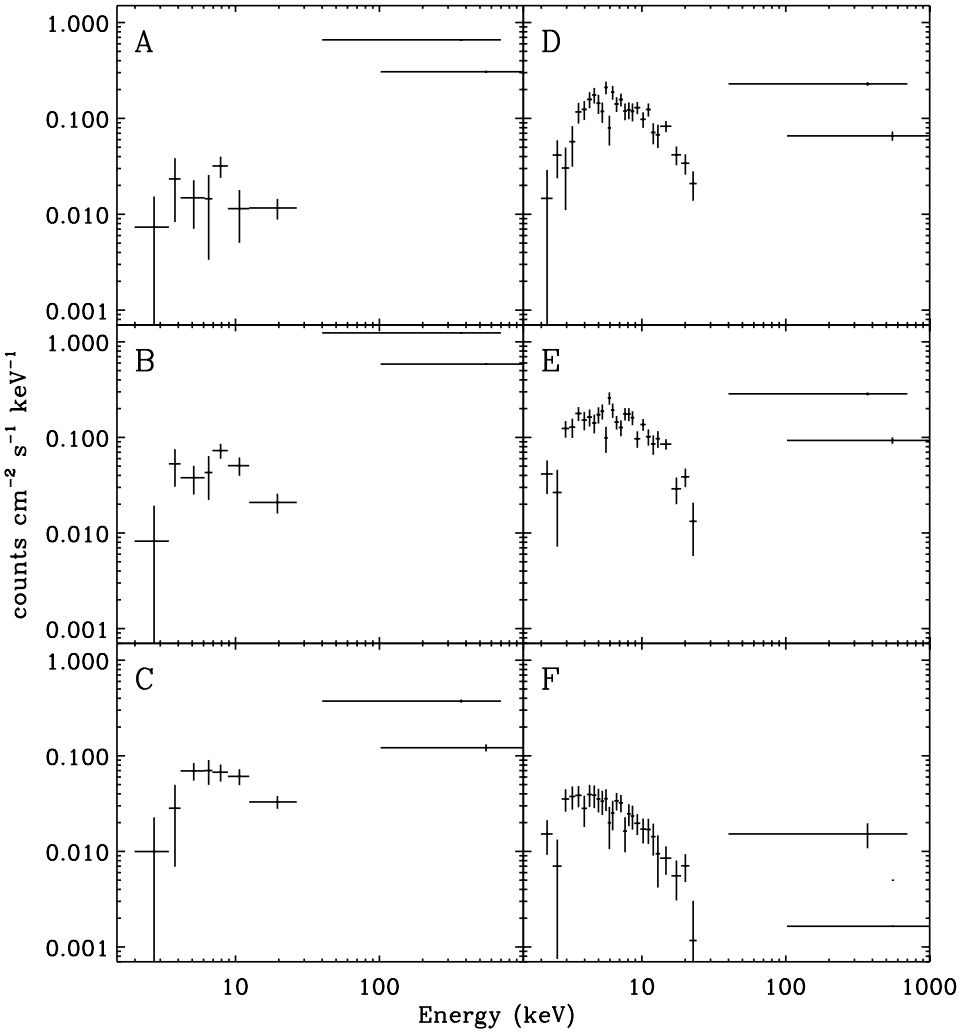

FIG. 3.—Count spectra of the burst in the time intervals A, B, C, D, E, and F. For the spectral fits, we summed together the spectra A, B, and C in order to constrain the model parameters.

TABLE 1
SPECTRAL PARAMETERS OF THE BKNPL AND CPL BEST-FIT MODELS

Interval	Model	$N_{\rm H}$ (10^{22} cm^{-2})	α	β	E_b (keV)	E_c (keV)	χ^2/dof	F-test [a]
ABC	BKNPL	[0.061]	$0.02^{+0.20}_{-0.24}$	$2.10^{+0.10}_{-0.20}$	46^{+12}_{-9}	...	11.2/5	...
	BKNPL	$13.1^{+18.8}_{-8.3}$	$0.54^{+0.42}_{-0.46}$	$2.13_{-0.22}$	56^{+99}_{-18}	...	5.6/4	0.12
	CPL	$14.9^{+12.6}_{-8.3}$	$0.36^{+0.24}_{-0.23}$	...	...	80^{+22}_{-18}	5.6/5	0.033
D.....	BKNPL	[0.061]	$0.26^{+0.18}_{-0.20}$	$2.28^{+0.26}_{-0.15}$	15^{+7}_{-3}	...	53/26	...
	BKNPL	$10.6^{+5.8}_{-4.1}$	$1.05^{+0.27}_{-0.24}$	$2.88^{+0.39}_{-0.37}$	36^{+12}_{-11}	...	28.7/25	1.2×10^{-4}
	CPL	$10.6^{+5.0}_{-4.0}$	$0.91^{+0.25}_{-0.25}$	...	...	55^{+23}_{-14}	28.8/26	2.6×10^{-5}
E.....	BKNPL	[0.061]	$0.64^{+0.11}_{-0.10}$	$2.66^{+0.28}_{-0.30}$	33^{+7}_{-7}	...	54.8/26	...
	BKNPL	$5.3^{+3.2}_{-2.5}$	$1.01^{+0.21}_{-0.20}$	$2.64^{+0.30}_{-0.28}$	39^{+12}_{-10}	...	40/25	5.2×10^{-3}
	CPL	$5.5^{+3.1}_{-2.4}$	$0.93^{+0.19}_{-0.19}$	...	...	67^{+21}_{-17}	40.6/26	2.4×10^{-3}
F	BKNPL	[0.061]	$1.02^{+0.18}_{-0.18}$	$4.2_{-2.8}$ [b]	38^{+23}_{-29}	...	15.6/26	...
	BKNPL	<4.2 (2 σ)	$1.27^{+0.36}_{-0.33}$	$4.6_{-3.1}$ [b]	51^{+35}_{-29}	...	13/25	0.24
	CPL	<4.4 (2 σ)	$0.95^{+0.50}_{-0.45}$	...	...	31^{+29}_{-12}	13.5/26	0.20
1.....	BKNPL	[0.061]	$0.37^{+0.15}_{-0.10}$	$2.26^{+0.22}_{-0.17}$	104^{+14}_{-13}	...	119/76	...
	BKNPL	$26.7^{+23.7}_{-15.6}$	$0.84^{+0.14}_{-0.15}$	$2.49^{+0.30}_{-0.24}$	130^{+17}_{-18}	...	105/75	2.1×10^{-3}
	CPL	$10.1^{+14.9}_{-8.0}$	$0.29^{+0.15}_{-0.14}$	...	...	103^{+16}_{-13}	98.9/76	8.0×10^{-2}
2.....	BKNPL	[0.061]	$0.58^{+0.09}_{-0.11}$	$2.24^{+0.13}_{-0.13}$	18^{+3}_{-4}	...	80.9/66	...
	BKNPL	$5.3^{+2.2}_{-1.9}$	$1.00^{+0.14}_{-0.14}$	$2.33^{+0.12}_{-0.13}$	33^{+6}_{-6}	...	60.7/65	1.6×10^{-5}
	CPL	$7.0^{+2.2}_{-1.8}$	$1.08^{+0.11}_{-0.10}$	...	...	81^{+18}_{-13}	56.2/66	5.5×10^{-12}

[a] The column reports the chance probability values obtained with the F-test.
[b] The 90% upper boundary value is unconstrained by the fit.

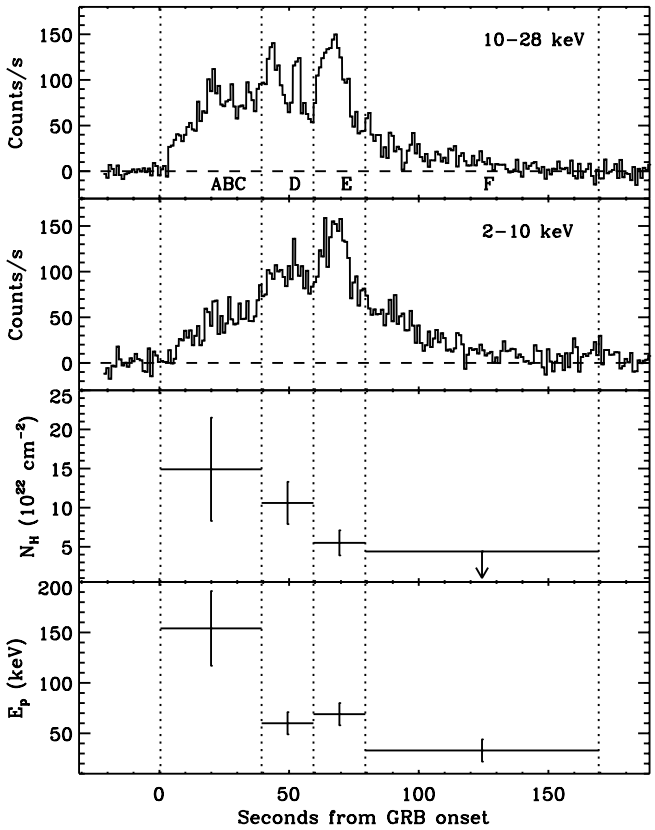

FIG. 4.—Time behavior of the hydrogen equivalent column density and peak energy of the EF(E) spectrum. The 2–10 keV and 10–28 keV light curves are also shown.

40–700 keV peak fluxes in the 1 s time bin are $F_{2-10} = 2.1 \times 10^{-8}$ ergs cm^{-2} s^{-1} and $F_{40-700} = 1.4 \times 10^{-6}$ ergs cm^{-2} s^{-1}, while the fluences are given by $S_{2-10} = 9.1 \times 10^{-7}$ ergs cm^{-2} and $S_{40-700} = 1.37 \times 10^{-5}$ ergs cm^{-2}, with a softness ratio SR $= S_{2-10}/S_{40-700} = 0.066$, which is a value typical of a classic GRB (e.g., Frontera et al. 2000). Finally the total 2–700 keV fluence of the GRB is given by $S_{2-700} = 1.9 \times 10^{-5}$ ergs cm^{-2}.

3.2. *Afterglow Emission*

Because of the weakness of the afterglow source (see Fig. 1), no statistically significant spectral information could be derived. Assuming the average power-law photon index (1.95) derived from the spectra of a large sample of GRB afterglows (Frontera 2003), from the MECS data we estimated the afterglow source flux in the two observations of GRB 000528 using an image extraction radius of 2′ and adopting the MECS standard background level. The resulting 2–10 keV mean flux is $(1.6 \pm 0.4) \times 10^{-13}$ ergs cm^{-2} s^{-1} (1 σ uncertainty) during ToO1 and less than 5.2×10^{-14} ergs cm^{-2} s^{-1} (2 σ upper limit) for ToO2. These fluxes can only give an upper limit to the fading rate of the afterglow source. Assuming a power law for the flux time behavior [$F(t) \propto t^{\delta}$] with time origin at the GRB onset, the 2 σ upper limit to δ is -0.74, which is not very constraining for the afterglow decay rate. Back-extrapolated to the time of the main event, this decay implies a flux much lower than that measured with the WFC. A tighter constraint on δ can be obtained with a reversed argument, imposing the condition that, as observed in many *BeppoSAX* GRBs (Frontera et al. 2000; Frontera 2003), the late part of the prompt emission is correlated with the late afterglow emission, pointing to the former as early afterglow. In Figure 5 we show the results. Assuming the GRB onset as the origin of the afterglow onset time, we find that the smooth GRB decay starting at the beginning of the time interval F in Figure 2 is consistent with a power law with index $\delta = -3.7 \pm 0.3$. As shown in Figure 5 (*left panel*), its

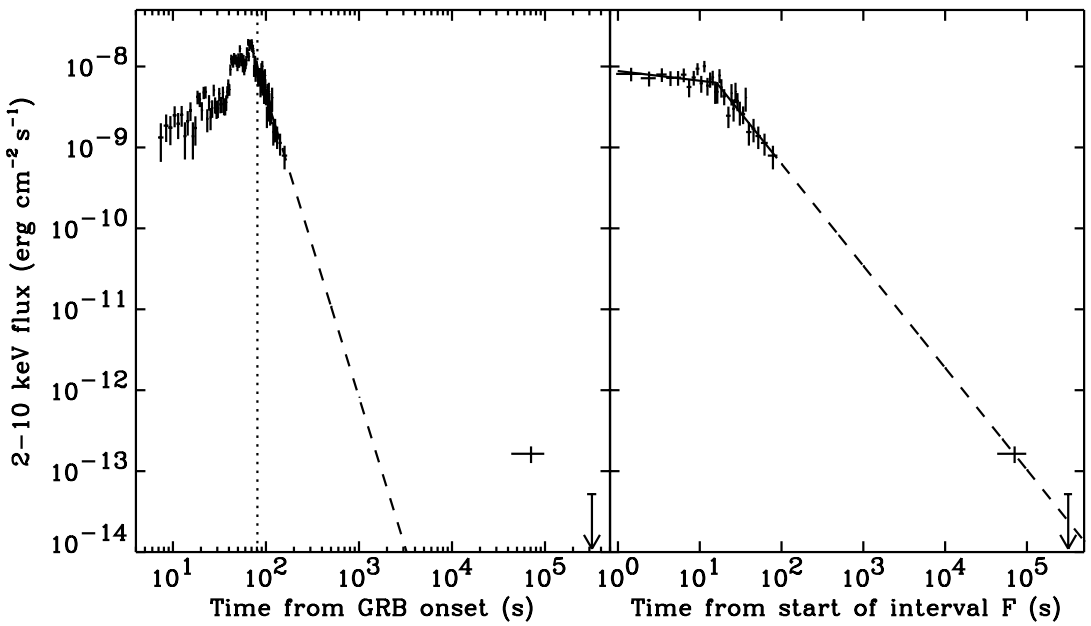

FIG. 5.—The 2–10 keV fading curve of GRB 000528. The afterglow upper limit is at the 2 σ level. The vertical dotted line in the left panel shows the beginning of the interval F. *Left:* Light curve of the GRB and its afterglow assuming the onset time of the GRB as the origin. The best fit of the light curve in the interval F and its extrapolation at later times is also shown. *Right:* Light curve in the interval F and its extrapolation at later epochs, when the beginning of the interval F is assumed as the origin of the afterglow onset time.

extrapolation to the time of the *BeppoSAX* NFI measurements gives a flux much lower than that measured. A different result is obtained if we fix as the origin of the time coordinate for the afterglow the beginning of the time interval F. In this case, the 2–10 keV smooth decaying flux is described by a broken power law (a simple power law is unacceptable, $\chi^2/\mathrm{dof} = 88/31$; see right-hand panel of Fig. 5) with best-fit parameters $\delta_1 = -0.12 \pm 0.06$, $\delta_2 = -1.33 \pm 0.13$, and break time $t_{\mathrm{break}} = 16^{+1.9}_{-2.5}$ s. We notice that the second power-law index is that typical of X-ray afterglows (Frontera 2003) and that, when this law is extrapolated to the epochs of the ToO1 and ToO2 measurements, it is found to be consistent with the afterglow fluxes measured at these times. All this suggests that the afterglow onset time is delayed by $\sim$80 s with respect to the GRB onset time and that the final fading of the early afterglow of GRB 000528 occurs about 16 s after a slower fading. Other cases of possible delayed afterglow onset have been reported (e.g., GRB 39510; Pian et al. 2001 and references therein).

4. DISCUSSION

Two main results have been obtained from the present analysis of the GRB 000528 *BeppoSAX* data: the evidence of an early afterglow with onset time delayed with respect to the GRB onset and the discovery of an absorption column density significantly higher than the Galactic value during most of the burst prompt emission with evidence of a decreasing behavior with time. We discuss both.

4.1. *The Early Afterglow*

The finding that, assuming as the time origin the beginning of interval F in Figure 2, the extrapolation of the fading law of the late prompt emission is consistent with the flux of the late afterglow is highly suggestive of the expectations of the internal-external shocks model during the fast cooling phase (Sari & Piran 1995, 1999).

The derived early afterglow decay law and the photon spectrum of the last interval F (see Table 1) confirm this scenario. Indeed, assuming a synchrotron emission, according to Sari & Piran (1999), the photon spectrum due to the fast cooling electrons is described by a set of four power laws, the first $N(E) \propto \nu$ for $\nu < \nu_{\mathrm{sa}}$, where ν_{sa} is the photon self-absorption frequency, the second $N(E) \propto \nu^{-2/3}$ for $\nu_{\mathrm{sa}} < \nu < \nu_c$, where ν_c is the cooling frequency, the third $N(E) \propto \nu^{-3/2}$ for $\nu_c < \nu < \nu_m$, where ν_m is the characteristic synchrotron frequency, and the last $N(E) \propto \nu^{-p/2-1}$ for $\nu > \nu_m$, where p is the index of the electron energy power-law distribution. Comparing these expectations with our spectral results in the interval F (broken power law with low-energy photon index $\alpha = 1.27^{+0.36}_{-0.33}$, high-energy photon index $\beta = 4.6_{-3.1}$, $E_{\mathrm{break}} = 51^{+35}_{-29}$), we can see that α is consistent with the expected power-law index (3/2) in the $\nu_c < \nu < \nu_m$ frequency band and thus that ν_m corresponds to E_{break}. Unfortunately, the high-energy photon index β is affected by a large uncertainty with the 90% upper boundary unconstrained, and thus it cannot be efficiently used to constrain p. However, p can be constrained by the measured light curve of the early afterglow.

Indeed, in the case of the fast cooling phase (Sari & Piran 1999), at X-ray frequencies, the energy flux $F(t)$ is expected to increase as t^2 for $t < t_\gamma$, where t_γ is the time in which the relativistic flow changes from a constant Lorentz factor into a decelerating phase, $F(t)$ is expected to decay as $t^{-1/4}$ for $t_\gamma < t < t_m$, where t_m is the time in which the typical synchrotron frequency cross the observed frequency, and finally $F(t)$ is expected to decay as $t^{1/2-3p/4}$ at later times ($t > t_m$). The light curve we observe is nicely similar to that expected; it has first a temporal index $\delta_1 = -0.12 \pm 0.06$, which is marginally consistent with that ($-1/4$) expected for $t < t_m$, then has a temporal index $\delta_2 = -1.33 \pm 0.13$, which, compared with that expected ($1/2 - 3p/4$), allows us to estimate $p = 2.44 \pm 0.17$. This value of p is consistent with the estimated high-energy photon index of the BKNPL.

Because of the thick shell regime, we are not able to directly observe the onset time of the afterglow and then to derive the initial Lorentz factor Γ_0 from the deceleration time of the fireball t_γ, which depends on Γ_0 (Sari & Piran 1999). An attempt to evaluate t_γ was made by fitting the GRB light curve in the interval F with a broken power law as above, in which δ_1 is frozen to $-1/4$ and the other parameters, δ_2, t_{break}, and the onset time t_0 of the afterglow with respect to the starting time of the interval F, were left free to vary. We found that the best fit is obtained with $t_0 = -3^{+2}_{-5}$ s, $\delta_2 = -1.29^{+0.11}_{-0.18}$, and $t_{\mathrm{break}} = 17^{+3}_{-1}$ s. The fading law obtained with these parameters is still nicely consistent with the late afterglow measured flux. From this result, following Sari & Piran (1999), we can get an estimate of the deceleration time t_γ ($t_\gamma = -t_0$) and then an estimate of Γ_0 if we know the GRB redshift. Placing GRB 000528 at $z = 0.5$ (see below for a discussion), we obtain $\Gamma_0 \sim 100 n_4^{-1/8}$, where n_4 is the density of the external medium in units of 10^4 cm^{-3}. We stress, however, that the derived value of these parameters should be taken as rough estimates because we adopted equations valid for an unperturbed interstellar medium, which are not strictly applicable to the thick-shell case. In addition, it is worth considering that, lacking a decay slope only constrained from NFI observations, other possible solutions could be considered. In spite of all this uncertainty, we consider the scenario outlined above plausible.

4.2. *The Column Density Behavior*

The other major result of the present spectral analysis of the GRB 000528 prompt emission is the detection of a hydrogen equivalent column density significantly higher than the Galactic value. Even if, as discussed, a constant value cannot be excluded, the likely temporal behavior of N_{H} is an exponential function with initial value $N_{\mathrm{H}}(0) \sim 2.4 \times 10^{23}$ cm^{-2} (assuming a redshift $z = 0$) and decay constant $t_0 \sim 50$ s. It is the second time, after the case of GRB 980329 (Frontera et al. 2000; Lazzati & Perna 2002), that N_{H} exhibited such time behavior, although evidences of variable absorption during the prompt emission of GRBs have already been reported (GRB 990705, Amati et al. 2000; GRB 010222, in 't Zand et al. 2001; GRB 010214, Guidorzi et al. 2003). As discussed in § 1, in the case of GRB 980329, the N_{H} behavior was found to be consistent with a photoionization process, which is expected when a GRB occurs within a cloud of initially cold gas. The cloud mass density was found to be $n \sim 4.5 \times 10^5$ cm^{-3} for a composition typical of interstellar matter, and the radial distribution was consistent either with a uniform sphere of radius $R_{\mathrm{sphere}} = 0.13$ pc or a shell at distance $R_{\mathrm{shell}} = 0.066$ pc and width $\Delta R = 0.1 R_{\mathrm{shell}}$. A marginal but not conclusive preference was given to the shell geometry (Lazzati & Perna 2002).

For GRB 000528 we tested the same model with two important improvements in the simulation of the photoionization process. First, we have taken into account the true gamma-ray light curve of the GRB, while in the case of GRB 980329 (Lazzati & Perna 2002) a constant flux was assumed to be

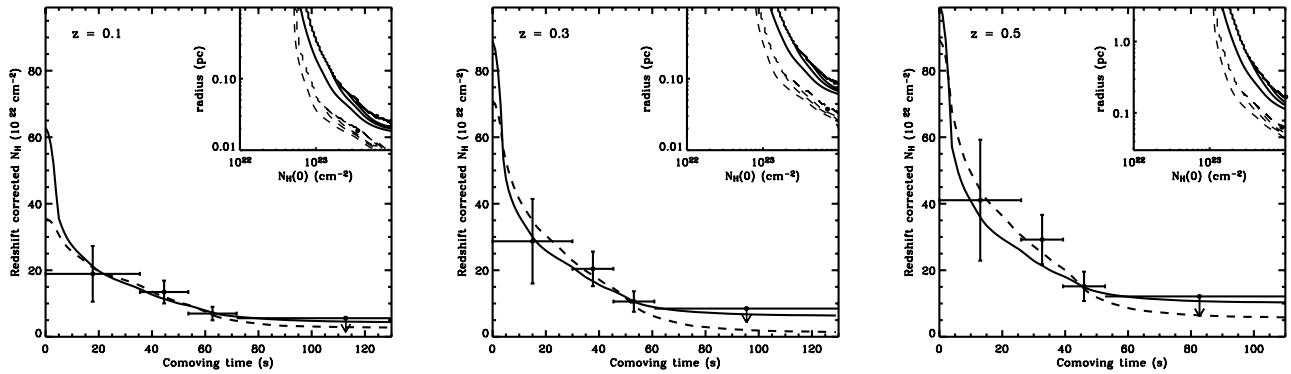

FIG. 6.—Redshift-corrected column density as a function of the time in the rest frame of the burst for three different assumed redshifts. Also shown is the best-fit model (see text) for the two cloud geometries: sphere (*continuous line*) and shell (*dashed line*). In the inset the corresponding best-fit values (initial redshift-corrected N_H and cloud radius) are shown for two geometries along with the 1 σ, 90%, and 99% confidence contours. The 90% and 99% contours are not closed.

incident on the cloud. Second, we have taken into account the cosmological effect on both the time dilation of the light curves and the measured column density; the fit was performed for three different values of z (0.1, 0.3, and 0.5). Consequently, the N_H values shown in Figure 4 were corrected to take into account the redshift effect on the column density according to the relation $N_H(z) = N_H(0)(1+z)^{2.5}$, which is valid in the redshift range $0 < z < 4$ (Lazzati & Perna 2002). The results of the model fit to the data are shown in Figure 6 and in Table 2 for the three values of z. From the χ^2 values shown in Table 2, in this case as well the two cloud geometries (sphere or shell) cannot be significantly disentangled, even if it appears again that there is a slight preference for the shell geometry. Assuming a spherical geometry, the radius of the cloud increases with z from 8.9×10^{16} to 5.0×10^{17} cm, while in the case of a shell, the shell distance increases with z from 5.6×10^{16} to 1.8×10^{17} cm (see Table 2). In addition, the initial column density is sensitive to the redshift assumed, ranging from 6.3×10^{23} to 1.0×10^{24} cm^{-2} in the first case and from 3.5×10^{23} to 8.9×10^{23} cm^{-2} in the second case.[11] However, independently of the redshift and cloud geometry, the best-fit values are all consistent with overdense regions of molecular clouds where star formation takes place, as also found for GRB 980329 (Lazzati & Perna 2002).

The amount of mass required to explain the variable absorption ranges between a few and a few hundred solar masses. This mass range is consistent with the masses ejected by Wolf-Rayet stars, the candidate progenitors of GRB explosions. If the mass were distributed as a wind, with an r^{-2} profile, most of the absorption would be at small radii, and the column density would be expected to vanish quickly. Lazzati & Perna (2002) simulated the evolution of absorption from a stellar wind, finding that even a Thomson-thick wind would vanish in less than a second (see their Fig. 6). This does not mean that our observations provide evidence against a stellar wind. It means that this kind of observation is not sensitive to the presence of a wind. Nevertheless, the observation can be interpreted as circumstantial evidence for the stellar origin of the progenitor. As recently discussed by Chevalier et al. (2004), the interaction of the wind with the surrounding interstellar medium (ISM) creates a dense and cold shell of material consistent with the shell inferred from our results.

[11] An initial column density larger than 10^{24} cm^{-2} has not been considered, since it would affect the γ-ray light curve of the GRB.

The above results suggest that the high density of the circumburst medium may be responsible for the unsuccessful search for an optical counterpart (Jensen et al. 2000, Palazzi et al. 2000). In most of the best-fit simulations (see Fig. 6), a sizable column density of the order of several $\times 10^{21}$ cm^{-2} remains after the GRB prompt phase has finished. Dust associated with this residual column density may well be responsible for the optical obscuration, even for a Galactic dust-to-gas ratio. In addition, Perna & Lazzati (2002) showed that depending on the cloud geometry and GRB spectrum, the dust to gas ratio at the end of the burst phase may be even larger than the initial one.

Remarkably, the temporal slope shown by the X-ray afterglow emission is typical of a GRB with constant density (Sari et al. 1998), which is the assumption for the cloud in the Lazzati & Perna (2002) model. We do not find evidence of a temporal break at least until 1 day from the main event. Moreover, the afterglow upper limit in ToO2 is consistent with the same temporal slope (see Fig. 5). If, in spite of that, we assume that a break in the light curve occurs 2 days after the burst, in the scenario of the internal-external shock model the break could be a consequence of a transition to a nonrelativistic phase of the shock (Dai & Lu 1999) due to a high-density medium. Using the Dai & Lu (1999) model, we can get an estimate of this density. Assuming a Lorentz factor $\gamma = 1$ at $t = 2$ days, from Dai & Lu (1999) we find that $E_{54} n_5^{-1/8} [(1+z)/2.6]^{3/8} = 0.65$, where E_{54} is the total isotropic-equivalent energy $E_{\rm rad}$ in units of 10^{54} ergs, n_5 is the medium density n in units of 10^5 cm^{-3}, and z is the GRB redshift. Assuming $z = 0.5$, which is also consistent with the minimum value inferred from the Amati et al. (2002) relation ($E_p - E_{\rm rad}$) for a 20%

TABLE 2

BEST-FIT PARAMETERS OF THE LAZZATI & PERNA (2002) MODEL FOR EVOLUTION OF THE COLUMN DENSITY

Cloud Geometry	Redshift	$N_H(0)$ (10^{23} cm^{-2})	Radius (pc)	χ^2/dof
Sphere.....	0.1	6.31	0.029	0.65
	0.3	8.91	0.086	0.55
	0.5	10.0	0.162	0.97
Shell	0.1	3.55	0.018	0.15
	0.3	7.08	0.036	0.35
	0.5	8.91	0.061	0.28

NOTE.—Error on the parameters is not quoted given the complex covariances (see Fig. 6).

dispersion of the data points around the best fit, for a standard cosmology with $H_0 = 71$ km s^{-1} Mpc^{-1}, $\Omega_m = 0.3$, and $\Omega_\Lambda = 0.7$ (Spergel et al. 2003), we find $E_{54} = 0.014$ and then a medium density of $n = 4.5 \times 10^4$ cm^{-3}. This value is somewhat smaller than the best-fit densities derived from the fit of the column density evolution. However, as shown in the insets of Figure 6, the data do not allow us to constrain the cloud geometry with high accuracy, and lower density solutions are consistent with the $N_{\rm H}$ evolution. In addition, given that late afterglow prevents us from inferring a fading law independently of the late prompt emission time behavior, we cannot exclude consistent afterglow solutions with a break before the first NFI observation, thus relaxing the upper limit on the ISM density. At any event, for the best-fit $N_{\rm H}$, the cloud geometry and density are consistent with the characteristics of massive cloud cores (Plume et al. 1997), and therefore with the progenitor being a massive, short-lived star.

Continuous, early time monitoring of the time-variable opacity (both in single lines and in continuum) has the potential to constrain the dependence of density on the radius (Lazzati et al. 2001b), and hence to trace the mass loss history of the progenitor star. These observations are expected to be partly covered by the upcoming satellite *Swift*, with its repointing capabilities of the X-ray and optical detectors in several tens of seconds. A mission that would be capable of fully monitoring the GRB opacity since the burst onset is the proposed Lobster-ISS for the *International Space Station*, a sensitive all-sky monitor with focusing optics from 0.1 to 3.5 keV (Fraser et al. 2002) paired with a GRB monitor for higher photon energies (from 2 keV to several hundreds of keV; Amati et al. 2004). When measurements of variable absorption in X-rays are complemented with those in the optical band, one can further put powerful constraints on the properties of dust in the environment of the burst (Perna et al. 2003).

We wish to acknowledge Jean in 't Zand for his help in the WFC data reduction. This research was supported by both the Italian Space Agency (ASI) and Ministry of the University and Research of Italy (COFIN funds 2003). *BeppoSAX* was a joint program of the Italian Space Agency and the Netherlands Agency for Aerospace Programs.

REFERENCES

Amati, L., et al. 2000, Science, 290, 953
———. 2002, A&A, 390, 81
———. 2004, Adv. Space Res., in press
Arnaud, K. A. 1996, in ASP Conf. Ser. 101, Astronomical Data Analysis Software and Systems V, ed. G. H. Jacoby & J. Barnes (San Francisco: ASP), 17
Band, D., et al. 1993, ApJ, 413, 281
Berezhiani, Z., Bombaci, I., Drago, A., Frontera, F., & Lavagno, A. 2003, ApJ, 586, 1250
Berger, E., & Frail, D. A. 2000, GCN Circ. 686, http://gcn.gsfc.nasa.gov/gcn3/686.gcn3
Bevington, P. R. 1969, Data Reduction and Error Analysis for the Physical Sciences (New York: McGraw-Hill), 195
Böttcher, M., Dermer, D. D., Crider, W., & Liang, E. P. 1999, A&A, 343, 111
Chevalier, R. A., Li, Z., & Fransson, C. 2004, ApJ, 606, 369
Connors, A., & Hueter, G. J. 1998, ApJ, 501, 307
Dai, Z. G., & Lu, T. 1999, ApJ, 519, L155
Fishman, G. J., et al. 1994, ApJS, 92, 229
Fraser, G., et al. 2002, Proc. SPIE, 4497, 115
Frontera, F. 2003, in Supernovae and Gamma-Ray Bursters, ed. K. W. Weiler (Berlin: Springer), 317
———. 2004, in ASP Conf. Ser. 312, Third Rome Workshop on Gamma-Ray Bursts in the Afterglow Era, ed. M. Feroci, F. Frontera, N. Masetti, & L. Piro (San Francisco: ASP), 3
Frontera, F., et al. 1997, A&AS, 122, 357
———. 2000, ApJS, 127, 59
———. 2004, ApJ, in press
Gandolfi, G. 2000, BeppoSAX Mail n. 00/10 and 00/11 (Rome: IASF), http://www.rm.iasf.cnr.it/ias-home/sax/obs000528.html
Guidorzi, C., Montanari, E., Frontera, F., & Feroci, M. 2000, GCN Circ. 675, http://gcn.gsfc.nasa.gov/gcn3/675.gcn3
Guidorzi, C., et al. 2003, A&A, 401, 491
Hjorth, J., et al. 2003, Nature, 423, 847
Hurley, K., Cline, T., Mazets, E., Frontera, F., Guidorzi, C., & Montanari, E. 2000, GCN Circ. 681, http://gcn.gsfc.nasa.gov/gcn3/681.gcn3
in 't Zand, J. J. M., et al. 2000, GCN Circ. 677, http://gcn.gsfc.nasa.gov/gcn3/677.gcn3
———. 2001, ApJ, 559, 710
Jager, R., et al. 1997, A&AS, 125, 557
Jensen, B.L., et al. 2000, GCN Circ. 674, http://gcn.gsfc.nasa.gov/gcn3/674.gcn3
Kuulkers, E., et al. 2000, GCN Circ. 700, http://gcn.gsfc.nasa.gov/gcn3/700.gcn3
Lazzati, D., Ghisellini, G., Amati, L., Frontera, F., Vietri, M., & Stella, L. 2001a, ApJ, 556, 471
Lazzati, D., & Perna, R. 2002, MNRAS, 330, 383
Lazzati, D., Perna, R., & Ghisellini, G. 2001b, MNRAS, 325, L19
Lazzati, D., Ramirez-Ruiz, E., & Rees, M. J. 2002, ApJ, 572, L57
Paczynski, B. 1998, ApJ, 494, L45
Palazzi, E., et al. 2000, GCN Circ. 691, http://gcn.gsfc.nasa.gov/gcn3/691.gcn3
Perna, R., & Lazzati, D. 2002, ApJ, 580, 261
Perna, R., Lazzati, D., & Fiore, F. 2003, ApJ, 585, 775
Perna, R., & Loeb, A. 1998, ApJ, 501, 467
Pian, E., et al. 2001, A&A, 372, 456
Piro, L., et al. 2000, Science, 290, 955
Plume, R., Jaffe, D. T., Evans, N. J., Martín-Pintado, J., & Gómez-González, J. 1997, ApJ, 476, 730
Sari, R., & Piran, T. 1995, ApJ, 455, L143
———. 1999, ApJ, 520, 641
Sari, R., Piran, T., & Narayan, R. 1998, ApJ, 497, L17
Spergel, D. N., et al. 2003, ApJS, 148, 175
Stanek, K. Z., et al. 2003, ApJ, 591, L17
Vietri, M., & Stella, L. 1998, ApJ, 507, L45